# RSC Advances

This article can be cited before page numbers have been issued, to do this please use: S. Li, C. Zhu, S. Guo and L. Guo, *RSC Adv.*, 2015, DOI: 10.1039/C5RA12025J.




ROYAL SOCIETY OF CHEMISTRY

www.rsc.org/advances

View Article Online
DOI: 10.1039/C5RA12025J

Journal Name

ARTICLE

# A dispersed rutile-$TiO_2$-supported Ni nanoparticle for enhanced gas production from catalytic hydrothermal gasification of glucose

Received 00th January 20xx,
Accepted 00th January 20xx

DOI: 10.1039/x0xx00000x

www.rsc.org/

Sha Li,[a] Chao Zhu,[a] Simao Guo[a] and Liejin Guo[*a,b]

Hydrothermal gasificition (HTG) is a promising technique for the utilization of wet biomass or organic wastes. This work reports a highly dispersed rutile-$TiO_2$-supported Ni nanoparticle synthesized by a sol-gel method and its catalytic performance for gas production ($H_2$ and $CH_4$) from HTG of glucose as a model compound of biomass. $NiTiO_3$ formation of the gel precursor during the calcination process demonstrated the enhanced interaction of Ni and $TiO_2$, and highly dispersive nickel crystallites were obtained after the reduction activation. Increase of the calcination temperature decreased the catalytic activity due to the sintering of nickel crystals. The supported Ni nanoparticle greatly promoted the carbon gasification efficiency of HTG of 10 wt.% glucose (glucose:Ni=1:0.11) from 27.1% to 68.7% at 400˚C, and from 48.2% to 96.4% at 600˚C in supercritical water. A highly active temperature region (400-500˚C) of nickel catalyzed methanation reaction for $CH_4$ formation was particularly confirmed. As the gasification was prolonged in supercritical water, the rutile-$TiO_2$-supported Ni nanoparticle showed stable crystalline structures and part of the deposited carbon was gasified. The regenerated catalysts also showed significant activities.

## 1. Introduction

Bioenergy offers significant possibilities for reducing the reliance on fossil fuels in energy industry due to its potential carbon neutral utilization[1] and renewable generation. A common feature of biomass is its moisture content, which is normally 10-60%, or higher, and water vaporization consumes much energy input when conventional gasification and fast pyrolysis are applied for its upgradation[2]. One promising process that could avoid the high drying cost of the moisture and realize efficient conversion of wet biomass to bio-fuels is hydrothermal gasification[2-8]. Properties of water (density, dielectric constant and ion product) change greatly when heated near or over its thermodynamic critical point (Tc=373.95˚C, Pc=22.064MPa), making itself behave as both liquid-like (e.g. high thermal conductivity[9]) and gas-like (e.g. high diffusivity [10]) media. Then a homogeneous single-phase medium for the miscibility of non-polar organic compound and efficient reactions of organics is provided, and also in which water performs both as the solvent and reactant. A gaseous product rich in $H_2$ and $CH_4$ could be obtained. This process is commonly termed hydrothermal gasification (HTG) or supercritical water gasification (SCWG) when operated in supercritical water (SCW: T>Tc, P>Pc).

In order to save the energy input and capital cost of this process, various kinds of homogeneous and heterogeneous catalysts were developed to promote the efficiency of HTG of real biomass or organic wastes at milder temperatures. Relative studies have been well reviewed elsewhere[2-8]. Nickel-based catalysts have been widely studied due to their efficient catalytic activities and low costs. Ni has been found active on C-C bond cleavage, facilitating the decomposition and gasification of organics by pyrolysis and steam reforming reactions[11]. Ni is also active on methanation and water-gas shift reactions[12-14] in SCW, leading to a gaseous product rich in $CH_4$ and $H_2$, and low in CO. So far in this research field, many studies focus on the screening or designing of supported Ni materials for higher catalytic performances, better hydrothermal stabilities and anti-carbon abilities for HTG of organics.

Elliott's group[15] screened several commercial supported Ni catalysts for the HTG of p-cresol using a stirred batch reactor. Ni/γ-$Al_2O_3$ showed the best activity. But their results of the evaluation of the supporting materials[15] showed that, γ-$Al_2O_3$ transformed to γ-AlO(OH) after the exposure to SCW, and only monoclinic $ZrO_2$, α-$Al_2O_3$, $SiO_2$ and $TiO_2$ were found unreactive in SCW. In the work performed by Azadi and Farnood[16], γ-$Al_2O_3$ also transformed into γ-AlO(OH) after being exposed to SCW at 380˚C for 1 h. In Xu's work[17], however, γ-$Al_2O_3$ of Ni/γ-$Al_2O_3$ catalyst prepared by the incipient wetness impregnation method exhibited a stable crystalline structure in the SCW after a time-on-stream of 5-10 h at 600˚C. These conclusions about the stability of γ-$Al_2O_3$ support alone or with Ni indicate that Ni probably plays a role in the phase transformation of γ-$Al_2O_3$ or other supports under SCW conditions. Minowa and co-workers[11] studied several commercial Ni catalysts supported by alumina, silica-alumina, aluminum silicate, silica, kieselguhr and magnesia for the decomposition of cellulose in hot-compressed water. Ni/MgO showed the highest activity, but it was severely deactivated due to the phase change of MgO to $Mg(OH)_2$ and coking[11, 12]. A co-precipitated Ni-Mg-Al catalyst with nickel

[a] State Key Laboratory of Multiphase Flow in Power Engineering, Xi'an Jiaotong University, Xi'an 710049, Shaanxi, China, E-mail: lj-guo@mail.xjtu.edu.cn; Telephone: +86-29-82663895; Fax: +86-29-82669033.
[b] College of Engineering, Department of Mechanical Thermal Engineering and Chemical & Material Engineering, King Abdulaziz University, P.O.Box 80257, Jeddah 21589, Saudi Arabia

View Article Online
DOI: 10.1039/C5RA12025J




crystals of about 9.4 nm was prepared by Li et al[12]. The Ni-Mg-Al sample showed very high activity for SCWG of glucose and stable crystalline structure after 20 min's reaction at 400˚C, but its porous structure suffered certain degree of sintering (surface area loss). Azadi and Farnood [16] tested 44 supporting materials for Ni for SCWG and found that α-$Al_2O_3$, $TiO_2$ and yttria-stabilized zirconia (YSZ) were stable after the exposure to SCW at 380˚C for 1 h. In their study[16], Ni/$TiO_2$ and Ni/YSZ prepared by the incipient wetness impregnation method achieved lower carbon conversions compared with Ni/α-$Al_2O_3$. A novel carbon-supported Ni catalyst was prepared by Sharma[18] using an ion exchange method. The highly dispersive Ni (2.8 nm and 4.0 nm) showed a steady activity during the long-term tests using phenol as feedstock. However, growth of nickel crystals was observed after the reaction. Gupta's group [19] prepared several Ni catalysts supported by $TiO_2$, $ZrO_2$ and $MgAl_2O_4$ by impregnation method for the SCWG of a bio-oil at 600˚C. They found that char formation rate was the smallest over Ni/$TiO_2$, but part of anatase-$TiO_2$ transformed into rutile/brookite form after the HTG reaction.

Based on the previous studies, rutile-$TiO_2$ (anatase form could be transformed to rutile form in SCW) was found unreactive under hydrothermal conditions[8, 16, 19]. However, as reviewed, there were just several screening studies on the impregnated $TiO_2$-supported Ni samples for SCWG[16, 19], specific design of $TiO_2$-supported Ni catalyst for HTG was very limited. Due to the tendency of $TiO_2$ to from strong-metal support interaction (SMSI) with transition metals, Rossetti's group[20-22] synthesized several $TiO_2$-supported Ni catalysts by impregnation and flame pyrolysis methods for steam reforming of ethanol and glycerol. They found that preparation procedure was a key parameter to establish the SMSI of the samples. In their studies[20-22], calcination at higher temperature (e.g. 800 ˚C of the impregnated sample) favoured the formation of a mixed oxide ($NiTiO_3$) in the catalyst precursors, which, after the activation, allowed the coexistence of more stable metallic Ni clusters of a higher catalytic activity within the supporting particles. In addition, Ni catalyses not only the steam reforming and pyrolysis reactions for the gasification of organics, but also the carbon formation which may cause the catalyst deactivation, and smaller Ni particle has been reported to be more resistant to carbon formation for steam reforming reactions[21-24]. Therefore, catalyst system which the active Ni highly disperses in rutile-$TiO_2$ support seems to have the research significance for HTG of organics. Hence herein, we tried to synthesize a dispersive $TiO_2$-supported Ni nanoparticle by a sol-gel method for HTG. Particularly, effluence of the calcination temperature of catalyst precursor on the interaction of the active phase and the support, and the effect of the resulted nickel dispersity on the catalytic activity were studied. Then the catalytic performance of the optimized rutile-$TiO_2$-supported Ni nanoparticle for the HTG of 10 wt.% glucose at a wide temperature range (200-600˚C in both sub- and supercritical water regions) was systematically evaluated. Hydrothermal stability and regeneration activity of the rutile-$TiO_2$-supported Ni nanoparticle were also investigated.

## 2. Experimental

### 2.1 Catalyst preparation

The $TiO_2$-supported Ni sample was synthesized by a complex-polymer sol-gel method using citric acid, nickel nitrate ($Ni(NO_3)_2{\cdot}6H_2O$) and tetrabutyl titanate ($Ti(OC_4O_9)_4$). Anhydrous ethanol was used as the solvent. All chemicals purchased from Sinopharm Chemical Reagent Co. Ltd. were of analytical grade and used without further purification. To form the initial sol, an ethanol solution dissolved with certain amount of citric acid was added dropwise into another ethanol solution containing 0.5 M $Ni(NO_3)_2{\cdot}6H_2O$ and 0.5 M $Ti(OC_4O_9)_4$, i.e. the weight ratio of Ni in the final sample was 42.3 wt.%. Molar ratio of citric acid to metallic cations ($Ni^{2+}$+$Ti^{4+}$) was 1:1. The mixed solution was stirred constantly at room temperature for 3 h, aged for 36 h, and then evaporated in a water bath at 80˚C for about 3 h. The obtained polymeric resin was dried at 120˚C for 12 h and thermally decomposed in a furnace under different set-temperatures (600 ˚C, 700 ˚C, 800 ˚C and 900 ˚C) with a dwell time of 3 h. These samples are referred to here after as NT600C (calcined at 600 ˚C), NT700C (calcined at 700 ˚C), NT800C (calcined at 800 ˚C) and NT900C (calcined at 900 ˚C), respectively. The calcined samples were ground, sieved with 200 meshes, and finally reduced by $H_2$ of a flow rate of 30 mL/min for 2.5 h. Before the HTG reaction, the reduced fresh catalysts were placed in airtight containers filled with argon.

For comparison with the crystalline structures and catalytic performances of the sol-gel samples, we also synthesized a rutile-$TiO_2$-supported Ni sample with the same nickel loading (42.3 wt.%) using incipient wetness impregnation method, which is referred as N-T600C. $TiO_2$ support of N-T600C was prepared by the same sol-gel process, and its annealing processes after having been impregnated with nickel nitrate were also the same with those of the optimized sol-gel sample.

### 2.2 Catalyst characterization

Crystalline structures of the samples were identified by X-ray diffraction (XRD) with a PANalytical X' pert MPD Pro diffractometer using Ni-filtered Cu Kα (wavelength 0.15406 nm) radiation X-ray tube, operated at 40 kV and 40 mA. For each sample, Bragg angles of 10-80˚ were scanned. Apparent average crystalline sizes of Ni were calculated by the Scherrer formula.

$H_2$ temperature programmed reduction (TPR) was carried out using the Auto Chem 2920 (Micromeritics Instrument Co.,USA) to determine the reducibility of the calcined precursors. Each sample was heated to 1000˚C with a heating rate of 10˚C/min in a mixed gas of 10 vol.% $H_2$ balanced with argon at a flow rate of 50 mL/min. $N_2$ adsorption/desorption of fresh and used catalysts were conducted at -196˚C on the ASAP 2020 (Micromeritics Instrument Co.,USA) to determine the pore structures. Prior to the measurement, samples were degassed at 300˚C for 300 min. Pore size distribution and specific surface area of the sample were determined by the Barrett-Joyner-Halenda (BJH) and Brunauer-Emmett-Teller (BET) methods, respectively.

Morphology of the catalysts was observed with a field emission scanning electron microscopy (SEM) (JEOL JSM-6700F) and a transmission electron microscopy (TEM) (Tecnai G2 F30, FEI, USA). For TEM analysis, sample was dispersed in ethanol, and then deposited on a Cu grid covered with a perforated carbon sheet.

Thermal decomposition behaviors of the polymeric resin precursors and coke over the used catalysts were analyzed by the temperature-programmed oxidation using a thermogravimetric analyzer (TGA:

View Article Online
DOI: 10.1039/C5RA12025J




SAT 499C, SICK). For each test, about 10 mg sample was heated in air at a flow rate of 30 mL/min from room temperature to 800˚C with a heating rate of 10˚C/min.

### 2.3 Evaluation of catalytic performance

HTG of glucose was performed in a mini-scale quartz tubing reactor (1.5 mm I.D., 3 mm O.D.), a kind of batch reactor that could eliminate the potential catalytic influence of metallic reactor walls. Glucose, as a model compound of biomass[25], was used as the feedstock. To prepare the reactors, certain amounts of 10 wt.% glucose aqueous solution and Ni catalyst were firstly loaded into the quartz tubes of one open-ended side with a syringe and a mini spoon. Then the quartz tubes were flamingly sealed. Weigh ratio of glucose to Ni in the feedstock was 1:0.11, and the water loading inside the quartz reactor was 122.32 kg/m$^3$. For the HTG reactions, the sealed reactors filled with feedstock were heated to the set-temperatures with a heating rate of 10˚C/min in a box-type furnace controlled by a rhodium-platinum thermocouple. Schematic diagram of the reaction heating system is shown as Fig 1(a). After a residence time of 20 min, the reacted quartz tubes were taken out and cooled naturally.

Fig 1(b) displays the gas sampling system. To obtain the gaseous product, the reacted quartz tube was placed inside a larger plastic tube (6 mm I.D.). The plastic tube was then filled with high-purity argon at ambient atmosphere and clamped by two clips at both ends. Subsequently, the inside reacted quartz tube was rapidly crushed into pieces by a plier, and the gaseous product inside the plastic tube mixed with argon could be extracted by a syringe and further measured. A gas chromatograph (Agilent 7890A) equipped with a thermal conductivity detector (TCD) was applied for the gas measurement. Gas yields were determined by the measured concentrations and the known argon amount. For each run, five quartz tubing reactors were carried out and their average values are presented.

Gas yield, carbon gasification efficiency (CGE) and hydrogen gasification efficiency (HGE) are considered as the indicators for the catalytic performance. Molar fractions of the gaseous products are also provided. Their formulas are listed as follows:

$$\text{Gas yield}=\frac{\text{mmol of gaseous products}}{\text{g of glucose}} \quad (1)$$

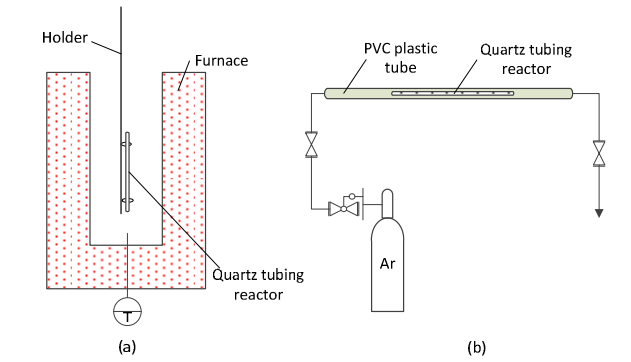


Fig. 1 Schematic diagrams of reaction heating system (a) and gas sampling system (b).

$$\text{CGE}=\frac{\text{carbon in the gaseous products}}{\text{carbon in the feedstock}}\times 100\% \quad (2)$$

$$\text{HGE}=\frac{\text{hydrogen in the gaseous products}}{\text{hydrogen in the feedstock}}\times 100\% \quad (3)$$

In order to address the properties of the used catalyst, a 500 mL autoclave (4575A, Parr Instrument Co., USA.) made of hastelloy was applied as a supplement of the quartz reactors, of which the samples were too little to be recovered. For each autoclave run, 50 mL water solution containing 5 wt.% glucose and 1.0 g catalyst was used as the feedstock. Heating rate of the autoclave was about 4˚C/min. The catalyzed HTG were carried out at 450˚C for different holding times with continuously stirring. The hydrothermally treated samples were collected and analyzed, but the gaseous products were not measured any more.

## 3. Result and Discussion

### 3.1 Variation of catalyst texture and structures

#### 3.1.1 Thermal analysis of the gel precursor

Calcination temperature greatly influences the interactions of the active metals and the supports[20, 22, 26, 27]. Thus before the calcination process of catalyst preparation, TGA and differential scanning calorimetry (DSC) were conducted to determine the thermal decomposition behavior of the polymeric resin precursor. $TiO_2$ was also synthesized and analyzed as a control. Fig. 2 shows the results. For both samples, the endothermic DSC regions of 70-240˚C corresponding to the rapid weight losses were mostly due to the evaporation of the residual ethanol solvent. In the higher exothermic temperature regions as shown, weight losses and DSC peaks are different between these two samples. For $TiO_2$, the exothermic region of 260-450˚C with peaks at 280˚C and 320˚C was probably associated with the decomposition and burnout of the organic matters in the gel, and the highest exothermic peak at 527˚C with a small weight loss could be ascribed to the burnout of some residual organic component, and probably the phase formation of rutile-$TiO_2$.

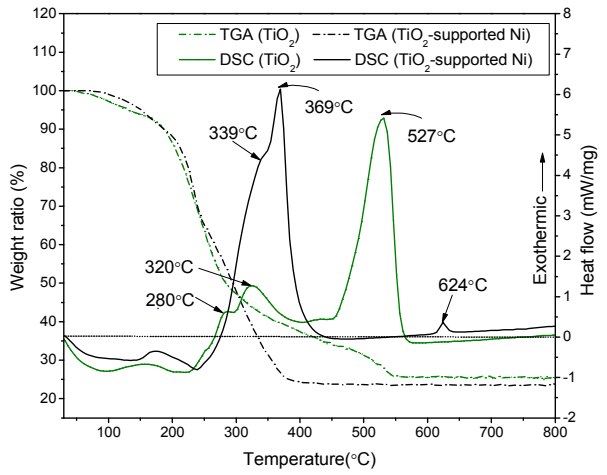


Fig. 2 TGA and DSC curves of the polymeric resin precursors of $TiO_2$ and $TiO_2$-supported Ni samples.

View Article Online
DOI: 10.1039/C5RA12025J




In the region of 255-460˚C of $TiO_2$-supported Ni sample, multiple exothermic peaks (the most intensive peak at 369˚C with a shoulder at 339˚C) were observed. Decomposition of nickel nitrate and burnout of the organic matters probably occurred around 339˚C. Then crystallization of anatase/rutile-$TiO_2$ and the starting formation of $NiTiO_3$ probably happened around 369˚C[26, 27]. The small exothermic peak of $TiO_2$-supported Ni sample at 624˚C with no weight change evidences the formation of more ordered $NiTiO_3$ at higher annealing temperatures[26]. Similar thermal decomposition behaviours of the polymeric resin precursors were observed by literatures[26, 27] when sol-gel methods were applied to prepare $NiTiO_3$ powders.

### 3.1.2 Crystalline structure and reducibility of the calcined catalyst precursors

It has been reported that higher calcination temperature could enhance the immersion of $Ni^{2+}$ into $TiO_2$ crystal lattices to form $NiTiO_3$ crystals, which, after activation, could allow the existence of Ni crystallites highly dispersed in the support[20-22, 26-28]. Preparation procedure is a key factor effecting on the formation of $NiTiO_3$. Rossetti's group[21, 22] prepared a $TiO_2$-supported Ni sample by incipient impregnation method and obtained the $NiTiO_3$ phase when calcined the precursor at 800˚C. When the direct sol-gel methods were applied, $NiTiO_3$ formation from the amorphous precursor was found to occur at the low temperature of about 600˚C [20, 26-29].

We calcined our gel precursors at 600˚C(NT600C), 700˚C(NT700C), 800˚C(NT800C) and 900˚C(NT900C), respectively, for 2 h, to explore the effect of the interaction of active metal and support on its catalytic activity for HTG, and to obtain more purified rutile-$TiO_2$ which has been found stable under hydrothermal conditions. The impregnated N-T600C sample was also calcined at 600˚C for 2 h. XRD patterns of the calcined catalyst precursors are displayed in Fig. 3. All sol-gel samples present similar characteristic diffraction peaks of rhombohedral $NiTiO_3$[26, 27, 30], NiO and rutile-$TiO_2$. N-T600C sample, however, just shows the individual intensive diffraction peaks of rutile-$TiO_2$ and NiO. The enhanced heating of the sol-gel samples resulted in the increased intensities of the diffraction peaks of all phases, indicating that there was a sintering of crystals under higher annealing temperatures. These results of the phase changings prepared by different methods are similar with the literature work mentioned above[20-22, 26-29].

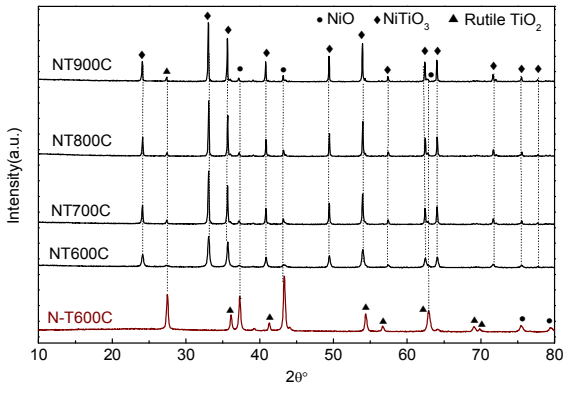


Fig. 3 XRD patterns of the calcined catalyst precursors.

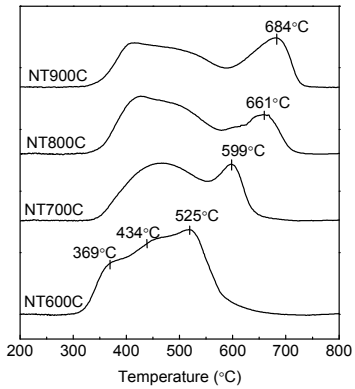


Fig. 4 TPR curves of the calcined sol-gel precursors.

Reducibility of the calcined sol-gel samples was measured by TPR technique and is depicted as Fig.4. For NT600C, peak at the lowest temperature of 369˚C could be assigned to the reduction of the bulk NiO, and the peak at 434˚C may represent the reduction of NiO interacting with $TiO_2$ as surface NiO-$TiO_2$[31]. The highest peak at 525˚C probably represents the less reducible $Ni^{2+}$ in $NiTiO_3$ particles[26]. As it can be seen in Fig.4, with the increase of the calcination temperature, reduction of $NiTiO_3$ species consumed more $H_2$ and the peak positions gradually shifted to higher temperatures, verifying that higher calcination temperature could enhance the formation and sintering of $NiTiO_3$, which is in accordance with the XRD results. Compared with $NiTiO_3$, the bulk and surface NiO species also consumed large quantities of $H_2$ during the TPR tests, indicating the substantial amounts of their existence in the samples. Prepared by impregnation[21, 22] or flame pyrolysis[21] methods, single TPR reduction peak of $NiTiO_3$ was obtained when the Ni loading was lower than 10 wt.%. Multiple TPR reduction peaks were obtained when the Ni loadings were 17 wt%[28] and 42.3 wt% (this work) using sol-gel methods. Therefore, besides the preparation methods, Ni loading amounts may also affect the $NiTiO_3$ contents in the calcined $TiO_2$-supported Ni samples. According to the XRD patterns in Fig.3, diffraction peaks of NiO of our sol-gel samples were extremely weak, showing that the NiO crystallites were still highly segregated in the calcined samples.

### 3.1.3 Crystalline and porous structures of the reduced catalysts

According to the results of the TPR tests, reduction activation of the oxide precursors was carried out at 600˚C, 650˚C, 700˚C and 750˚C for NT600C/N-T600C, NT700C, NT800C and NT900C, respectively. Fig. 5 displays the XRD patterns of the reduced samples. All patterns show the same characteristic diffraction peaks of Ni and rutile-$TiO_2$, and again, intensities of diffraction peaks of the sol-gel samples increased with the increased annealing temperature. N-T600C, as it can be seen, shows the most intensive diffraction peaks of reduced Ni. Calculated crystalline sizes of Ni are listed in Table 1. N-T600C showed the largest nickel crystals of 71.5 nm, and the sol-gel samples showed the increased crystalline sizes of Ni from 30.6 nm to 53.1 nm with the increased annealing temperature.

$N_2$ adsorption/desorption isotherms and pore size distributions of the fresh sol-gel catalysts are displayed as Fig. 6(a). All samples

View Article Online
DOI: 10.1039/C5RA12025J




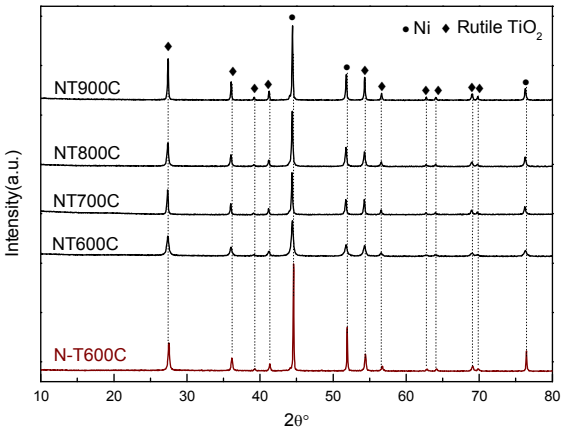


Fig. 5 XRD patterns of the reduced catalysts.

exhibit the physisorption isotherms of Type II and hysteresis loops of Type H1[32], indicating a non-porous or macroporous structure of the catalyst particles. Increased annealing temperature of samples gradually decreased the pore volume and enlarged the pore width of the catalysts as shown in Fig.6(a) and Table 1, illustrating the sintering of samples under higher annealing temperatures.

### 3.1.4 Morphology

Fig. 7 displays the SEM images and particle size distributions of the fresh samples. Growth of the nanoparticles with the enhanced annealing temperature can be observed, which is in accordance with the previous analysis of crystalline and porous structures. Particle sizes of NT600C and NT700C were concentrated in the range of 20-80 nm, and increased to larger ones up to 200 nm of NT800C and 400 nm of NT900C with the enhanced heat treatment. TEM images of NT600C are also displayed in Fig. 7. Nanoparticles of 20-60 nm

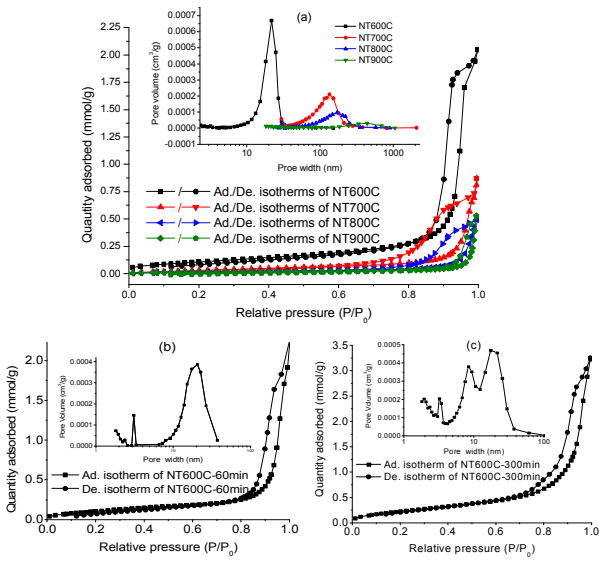


Fig. 6 $N_2$ adsorption/desorption isotherms and pore width distributions of fresh and used rutile-$TiO_2$-supported Ni catalysts.

Table 1. Nickel crystallite sizes and pore properties of fresh and used catalysts.

| Catalysts | Crystallite size of Ni (nm) | BET surface area ($m^2$/g) | Pore volume ($cm^3$/g) |
|---|---|---|---|
| N-T600C | 71.5 | | |
| NT600C | 30.6 | 13.5 | 0.07 |
| NT700C | 41.8 | 7.8 | 0.03 |
| NT800C | 46.2 | 3.9 | 0.02 |
| NT900C | 53.1 | 2.0 | 0.02 |
| NT600C-60min | 29.4 | 13.6 | 0.06 |
| NT600C-300min | 32.6 | 29.8 | 0.11 |

with irregular particle surfaces are observed.

### 3.2 Catalytic activity

### 3.2.1 Control experiments

Distributions of gas yields, CGE and HGE of HTG of 10 wt.% glucose at 400˚C catalyzed by $TiO_2$, N-T600C, NT600C, NT700C, NT800C and NT900C are displayed as Fig. 8. Non-catalytic run was also carried out for comparison. $TiO_2$ obtained the most same gas yields, CGE and HGE as the non-catalytic run, indicating the inactivity of rutile-$TiO_2$ for SCWG of glucose. NT600C achieved the highest total gas yield of 31.4 mmol/g, 2.2 times higher than that (9.8 mmol/g) without catalyst. NT700C, NT800C and NT900C, nevertheless, showed the gradually decreased activity. NT900C still exhibited a significantly higher activity than N-T600C.

As shown in Fig.8, without catalyst, abundant CO was produced due to the pyrolysis of the glucose intermediates[33]. When catalyzed

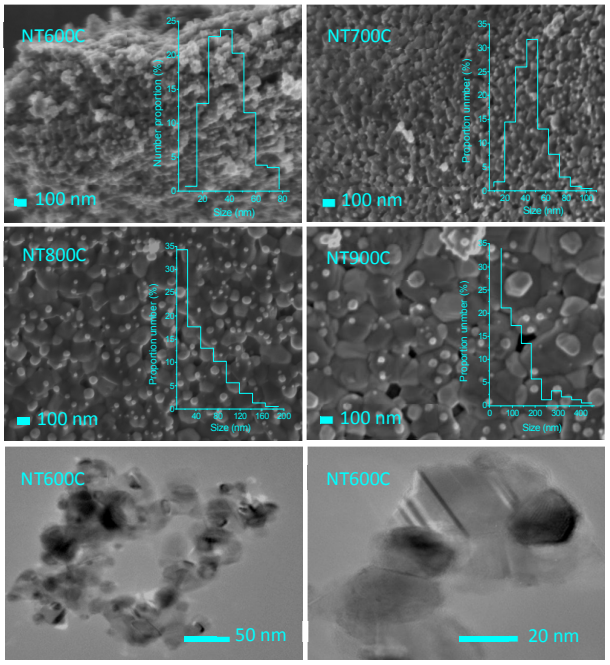


Fig. 7 SEM/TEM images and particle size distributions of fresh rutile-$TiO_2$-supported Ni nanoparticles.

View Article Online
DOI: 10.1039/C5RA12025J


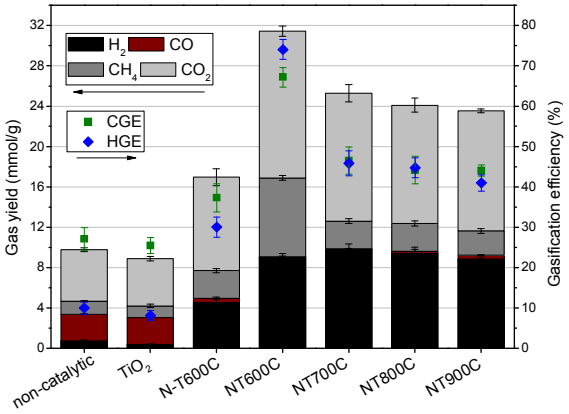


Fig. 8 Gas yields, CGE and HGE of non-catalytic and catalytic SCWG of 10 wt.% glucose at 400˚C (glucose : Ni=1:0.11; water density=122.32 kg/m$^3$).

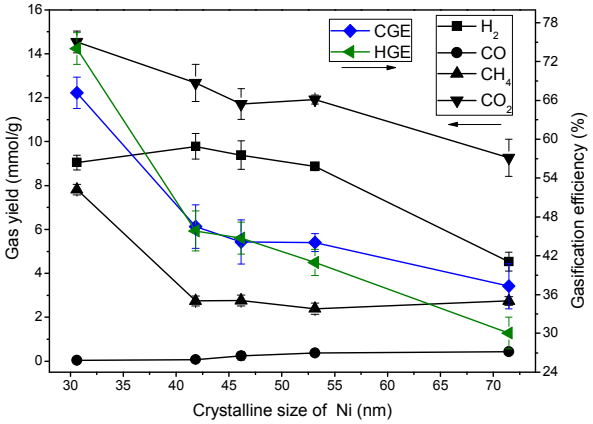


Fig. 9 Effect of the nickel crystalline size on the catalytic activity of rutile-$TiO_2$-supported Ni catalysts for SCWG of 10 wt.% glucose at 400˚C (glucose : Ni=1:0.11; water density=122.32 kg/m$^3$).

by nickel, the CGE and HGE were significantly improved, demonstrating the high activity of Ni on C-C cleavage for the enhanced decomposition of glucose and its intermediates. Then, particularly, the increased yields of $CH_4$ and $H_2$ and the remarkably decreased yields of CO demonstrated the active water gas shift reaction (WGSR, R1) and methanation reaction (R2) for CO conversion catalyzed by Ni.

$$CO+H_2O \xleftrightarrow{Ni} H_2+CO_2 \quad (R1)$$

$$CO+3H_2 \xleftrightarrow{Ni} CH_4+H_2O \quad (R2)$$

### 3.2.2 Effect of nickel dispersion

According to the XRD results, the sol-gel samples prepared under different annealing conditions went through the similar phase changes. Particularly, the formation of $NiTiO_3$ that was not found in the impregnated sample during the calcination process, illustrated the enhanced dispersion of Ni within the supports of the sol-gel samples. One observed change from the results of XRD, $N_2$ adsorption/desorption and SEM, was the aggregation/sintering of the nanoparticles with the increased annealing temperatures. Fig. 9 demonstrates the effect of nickel crystalline size on its catalytic activity. With the increase of the nickel crystalline size: a) $CO_2$ yield gradually decreased; b) CO yields increased; c) $H_2$ yield increased firstly then decreased; d) $CH_4$ yield decreased; e) CGE and HGE decreased. For the less sintered nanoparticles annealed at lower temperatures, there might be more active sites over the smaller nickel crystallites for the nickel catalyzed WGSR (R1) and methanation (R2) reactions, resulting in the higher yields of $CH_4$ and lower yields of $H_2$ and CO. Smaller nickel crystallites with more surface active sites also achieved higher gasification efficiencies by the enhanced decomposition (pyrolysis and steam reforming) of the organic intermediates. N-T600C had the largest nickel crystals, i.e. the lowest degree of nickel dispersion within the support, showed the lowest catalytic activity.

Preparation methods and nickel loading amounts may affect the dispersity of Ni and the catalytic performance. Azadi et al[16] prepared four kinds of $TiO_2$-supported Ni samples by incipient wetness impregnation method for SCWG of glucose using an autoclave reactor. Table 2 compares the results of the this work with those of Azadi's (results with the highest CGE)[16]. For our work as shown, with the same nickel loading, the optimized sol-gel rutile-$TiO_2$-spported Ni nanoparticle of a smaller nickel crystalline size achieved much higher catalytic activity than the impregnated sample. Despite of the potential catalytic activity of the metallic reactor[33] of Azadi's work, the sol-gel nanoparticle(NT600C) in this work obtained a higher CGE of much more concentrated glucose with much less nickel feedstock amount. Higher $CH_4$ yield and less $H_2$ yield of this work also indicate more active nickel sites of the sol-gel nanoparticles than the impregnated sample, due to the nickel catalyzed mathantion reaction (R2). These comparisons also suggest that for a better activity for HTG, it is crucial to develop dispersive

Table 2. Catalytic performances of $TiO_2$-supported Ni catalysts for SCWG of glucose

| | This work | This work | Azadi et al[16] |
|---|---|---|---|
| reactor material | quartz | quartz | stainless steel |
| temperature/˚C | 400 | 400 | 380 |
| catalyst preparation | wetness impregnation | sol-gel | wetness impregnation |
| nickel loading/wt.% | 42.5 | 42.5 | 5.0 |
| feedstock | 10 wt.% glucose | 10 wt.% glucose | 2 wt.% glucose |
| Ni: feedstock (g:g) | 0.11 | 0.11 | 0.25 |
| $H_2$ yield (mmol/g) | 4.5 | 11.6 | 16.7 |
| CO yield (mmol/g) | 0.4 | 0.4 | 0.6 |
| $CH_4$ yield (mmol/g) | 2.7 | 6.9 | 3.5 |
| $CO_2$ yield (mmol/g) | 9.3 | 15.8 | 15.6 |
| CGE/% | 37.3 | 69.2 | 59.1 |

View Article Online
DOI: 10.1039/C5RA12025J




nickel crystals, especially when the metal loadings are high, using more mixed precursors with titanium oxides.

### 3.2.2 Effect of temperature

Besides catalyst, temperature is also one of the most important operating parameters of HTG. Herein, we evaluated the HTG of glucose at a wide temperature range of 200-600˚C, to obtain a comprehensive understanding of the effects of both temperature and catalyst on the gas formation. Distributions of catalytic (NT600C) and non-catalytic gas yields, CGE, HGE and gas molar fractions are displayed as Fig. 10.

In subcritical water without catalyst as shown in Fig. 10(a), gas products were composed of $CO_2$ of the highest amount, trace amounts of $H_2$ and $CH_4$, and increased CO with the increase of temperature. In SCW region with the increased temperature, yields of $CH_4$, $H_2$ and $CO_2$ gradually increased, while yields of CO lineally decreased. Changing trends of yields of $CO_2$, $CH_4$, $H_2$ and CO of this work are consistent well with the results of Savage group [33-35] who carefully evaluated the effects of process variables on SCWG (365-600˚C) of cellulose and lignin using quartz tubing reactors. Their highest CO yield was obtained at 500˚C[33], which was 400˚C of our work, and this difference was probably due to the different heating methods and reaction holding times.

Compared with the non-catalytic gasification, gas yields catalyzed by NT600C were greatly promoted as shown in Fig. 10(b). In the whole temperature region, $CO_2$ was still the most abundant product while CO contents were almost undetectable. In subcritical water region, $H_2$ yields were significantly promoted by NT600C and dramatically increased with the increase of temperature. $CH_4$ yields however, increased slowly in subcritical water. In SCW region, yields of $H_2$ and $CH_4$ showed conversely changing trends at the temperature range of 400-550˚C: $CH_4$ yield dramatically increased in 400-500˚C, and then decreased with the further increase of temperature; $H_2$ yield decreased to be lower than $CH_4$ in 400-500˚C, and then dramatically increased with the further increase of temperature. As discussed, the low CO yields should be ascribed to the high activity of nickel on WGSR and methanation reactions. In subcritical water due to the significant $H_2$ yields and low $CH_4$ yields, the Ni catalyzed WGSR was probably more prominent than methanation reaction. In SCW region, the Ni catalyzed methanation reaction should be very active at 400-500˚C, resulting in the great formation of $CH_4$ and dramatic reduction of $H_2$. At 500-600˚C, $H_2$ yields thermodynamically increased with the increased temperature[36].

CGE and HGE of the HTG of glucose were greatly improved by NT600C as shown in Fig. 10(a) and Fig. 10 (b). The catalyzed CGE of 10 wt.% glucose was 86.1% at 450˚C and reached to 96.4% at 600˚C, which were only 34.4% and 48.2% of the non-catalytic runs, respectively. The catalyzed HGE was 98.5% at 450˚C and exceeded 100% when the temperature was further increased, verifying that the SCW also performs as a hydrogen source for the gas formation. Fig. 10(c) displays the non-catalytic and catalytic gas molar fractions under different temperatures. As it can been seen, Ni effectively decreased the concentrations of $CO_2$ and CO, and dramatically increased the $H_2$ concentrations in the gaseous products. Due the active Ni catalyzed methanation reaction, $H_2$ contents went through a reducing period during 400-500˚C.

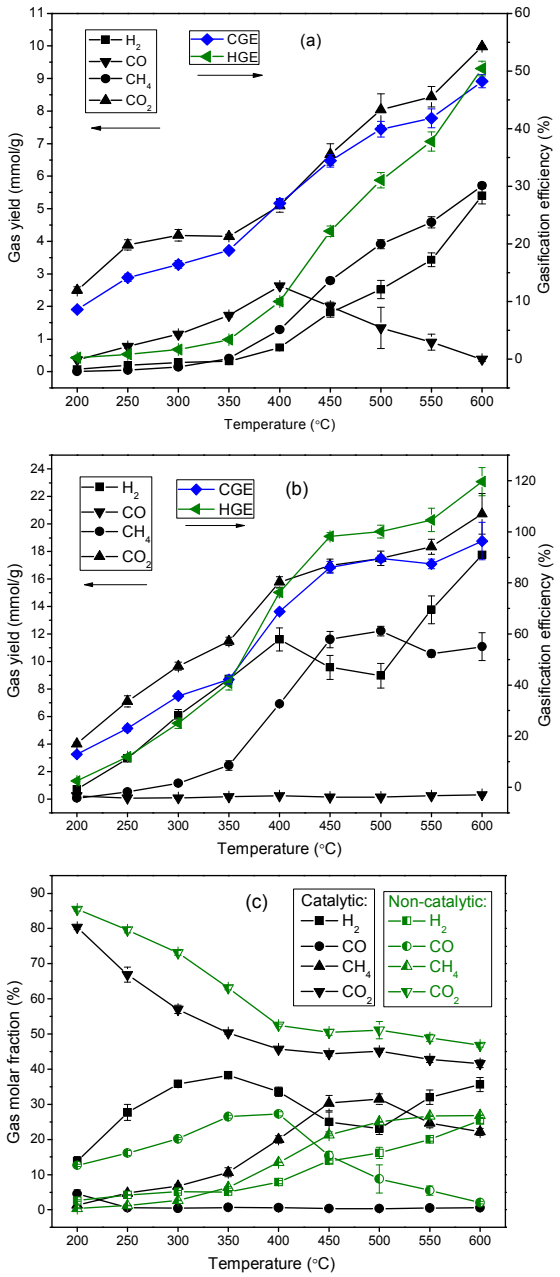


Fig. 10 Effect of temperature on gas yield, CGE, HGE and gas molar fraction of HTG of 10 wt.% glucose (a: non-catalytic gas yield, CGE and HGE; b: gas yield, CGE and HGE catalyzed by NT600C; c: non-catalytic and catalytic gas molar fractions; glucose: nickel =1:0.11; water density=122.32 kg/m$^3$).

### 3.3 Hydrothermal stability and regeneration activity

Sintering, phase changing of nickel/supports [4, 9, 37-39] and coking [40, 41] may deactivate Ni catalysts for HTG of organic feedstock. Therefore, we hydrothermally treated the most active rutile-$TiO_2$- supported Ni nanoparticle (NT600C) in SCW at 450˚C for 60 min

View Article Online
DOI: 10.1039/C5RA12025J




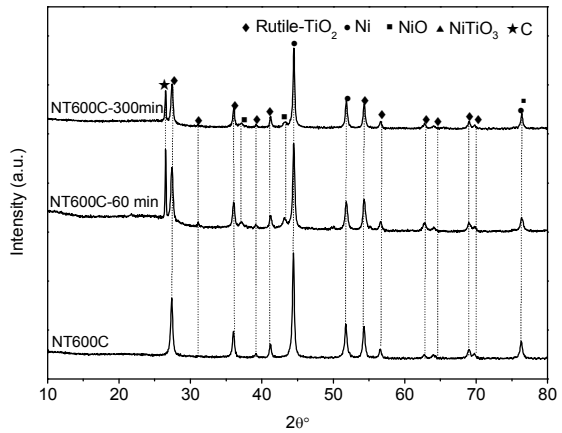


Fig. 11 XRD patterns of fresh and hydrothermally heated rutile-$TiO_2$-supported Ni catalysts.

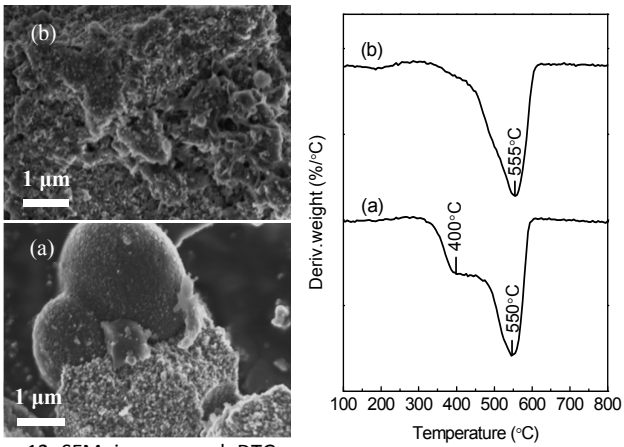


Fig. 12 SEM images and DTG curves of the hydrothermally heated NT600C catalyst at 450˚C for 60 min (a) and 300 min (b).

and 300 min, respectively, to examine the varied properties of the used catalysts. The collected samples are referred as NT600C-60min (hydrothermal heated for 60 min) and NT600C-300min (hydrothermal heated for 300 min), respectively.

#### 3.3.1 Crystalline structure of the used catalysts

Fig. 11 shows the XRD patterns of the fresh and hydrothermally treated rutile-$TiO_2$-supported Ni nanoparticle (NT600C). Compared with the fresh sample, there were two new phases of the used ones: the crystallized carbon at 2θ angle of 26.5˚ and NiO of week diffraction peaks at 2θ angle of 37.2˚, 43.3˚ and 75.5˚. Interestingly, intensity of the diffraction peak of the crystallized carbon decreased when the reaction was further prolonged. Amount of the deposited carbon, according the TGA results (section 3.3.2), decreased when the reaction was extended from 60 min to 300 min, indicating the probable gasification of the deposited carbon in SCW under longer running time. It is noted that intensities of the diffraction peaks the produced NiO in SCW were not increased with the increased reaction time, thus there should be no further oxidation of nickel crystals. Rutile-$TiO_2$ and Ni shows stable characteristic diffraction peaks as shown. Crystalline size of NT600C-60min was 29.4 nm, almost the same with that (29.7 nm) of the fresh NT600C, and it slightly grew to 32.6 nm when the reaction was extended to 300 min.

#### 3.3.2 Carbon deposition and pore structure of the used catalysts

SEM images of the used NT600C are displayed in Fig 11, adhering bulk carbons could be observed. DTG curves of used samples were also displayed in Fig. 12. For NT600C-60 min, there are two regions of the oxidation: one starts at around 380˚C and lasts to about 500˚C; the other has a peak valley around 550˚C. Peak at the higher temperature was probably attributed to the oxidation of the crystallized carbon detected by the XRD. Then the lower peak region could be ascribed as the oxidation of the amorphous carbon over the used catalyst. As shown in Fig. 12, the lower oxidation peak of NT600C-300min dramatically decreased compared with NT600C-30min. Total carbon amount over per gram catalyst decreased from 1.03 g of NT600C-60min to 0.70 g of NT600C-300min. Therefore, it could be indicated that part of the deposited carbon was gasified under hydrothermal conditions probably with the aid of rutile-$TiO_2$-supported Ni catalyst.

According to the TGA results, we calcined the reacted samples in air at 600˚C for 1 h to erase the deposited carbon before the $N_2$ adsorption/desorption tests. BET surface area and pore volume of the used catalysts are listed in Table 1, and the adsorption/desorption isotherms and pore size distributions are displayed as Fig. 6(b) and Fig. 6(c). Smaller pore width around 5 nm of NT600C-60min was formed, accompanying with the slight increase of the surface area compared with the fresh sample. For NT600C-300min, pore width around 8 nm was further formed, and its BET surface area and the pore volume obviously increased compared with those of NT600C. These changes of the pore structures were probably related with the oxidation of nickel within the nanoparticles and the gasification of the deposited carbon during the reaction in SCW.

#### 3.3.3 Regeneration activity

Regeneration of the used catalysts was carried out by reducing the calcined used samples at 600˚C with a $H_2$ flow of 30 mL/min for 2.5 h. Catalytic performances of the fresh and regenerated catalysts are shown in Fig. 13. Activity recovery rate of rutile-$TiO_2$-supported Ni nanoparticle slightly decreased with the increase of the exposure time in SCW. CGE of 10 wt. % glucose at 400˚C catalyzed by NT600C was 67.2%, and it decreased to 48.3% and 44.8% catalyzed by the regenerated NT600C-30min and NT600C-300min, respectively, which were still significantly higher than that (27.1%) of the non-catalytic run.

## 4. CONCLUSIONS

A dispersed rutile-$TiO_2$-supported Ni nanoparticle was synthesized by a sol-gel method for gas production ($H_2$ and $CH_4$) from hydrothermal gasification (HTG) of glucose. Enhanced interaction of Ni and rutile-$TiO_2$ prepared by the sol-gel method was demonstrated

View Article Online
DOI: 10.1039/C5RA12025J


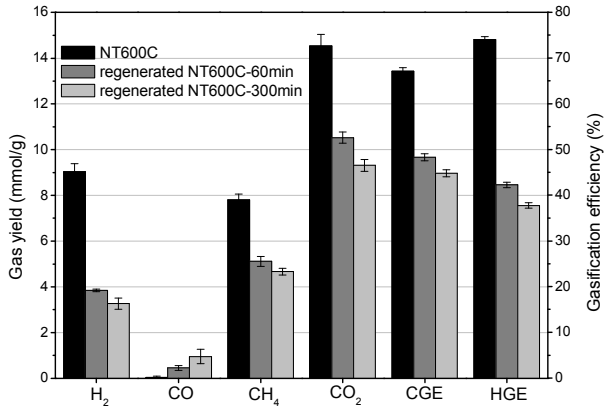


Fig. 13 Catalytic activity of regenerated rutile-$TiO_2$-supported Ni catalysts for hydrothermal gasification of 10 wt.% glucose at 400˚C (glucose: nickel=1:0.11; water density=122.32 kg/$m^3$).

by the formation of their mixed oxide ($NiTiO_3$) during the calcination process. Calcination temperature of 600˚C was sufficient to obtain the highly dispersive Ni within pure rutile-$TiO_2$ support, while increase of the calcination temperature caused the sintering of the nanoparticle and lowered its catalytic activity.

With the aid of the synthesized rutile-$TiO_2$-supported Ni nanoparticle, carbon gasification efficiency of HTG of 10 wt.% glucose (glucose:Ni=1:0.11) was significantly promoted from 27.1% to 68.7% at 400˚C, and from 48.2% to 96.4% at 600˚C in SCW. The hydrogen gasification efficiency was also greatly promoted from 10.0% to 76.3% at 400˚C, and from 50.4% to 119.7% at 600˚C in SCW. A highly active temperature region (400-500˚C in SCW) of nickel catalyzed methanation reaction for $CH_4$ formation was particularly confirmed.

Partial Ni of the rutile-$TiO_2$-supported Ni nanoparticle was oxidized in supercritical water. When the reaction time was extended to 300 min, Ni and rutile-$TiO_2$ showed stable crystalline structures, and no further oxidation of Ni was observed. In addition, gasification of deposited carbon over the used catalyst probably happened when the gasification was prolonged. The regenerated catalysts still showed significant activities. Totally, the sol-gel rutile-$TiO_2$-supported Ni nanoparticle exhibited high activity and potential stability and anti-carbon ability for long-term HTG of organics for clean gas production.

## Acknowledgements

Authors acknowledge the financial support from the National Key Project for Basic Research of China (973) No. 2012CB215303.

## Notes and references

1 I. Dincer, *Int. J. Hydrogen Energy*, 2002 **27**, 265-285.
2 A. A. Peterson, F. Vogel, R. P. Lachance, M. Fröling, J. M. J. Antal and J. W. Tester, *Energy Environ. Sci.*, 2008, **1**, 32-65.
3 P. Azadi and R. Farnood, *Int. J. Hydrogen Energy*, 2011, **36**, 9529-9541.
4 D. C. Elliott, *Biofpr*, 2008, **2**, 254-265.
5 L. Guo, Y. Lu, X. Zhang, C. Ji, Y. Guan and A. Pei, *Catal. Today*, 2007, **129**, 275-286.
6 Y. Guo, S. Z. Wang, D. H. Xu, Y. M. Gong, H. H. Ma and X. Y. Tang, *Renew. Sust. Energ. Rev.*, 2010, **14**, 334-343.
7 Y. Matsumura, T. Minowa, B. Potic, S. Kersten, W. Prins, W. Vanswaaij, B. Vandebeld, D. Elliott, G. Neuenschwander and A. Kruse, *Biomass Bioenergy*, 2005, **29**, 269-292.
8 T. M. Yeh, J. G. Dickinson, A. Franck, S. Linic, L. T. Thompson Jr and P. E. Savage, *J Chem Technol Biot*, 2013, **88**, 13-24.
9 N. Boukis*, V. Diem, U. Galla and E. Dinjus, *Combust. Sci. Technol.*, 2006, **178**, 467-485.
10 A. Loppinet-Serani, C. Aymonier and F. Cansell, *ChemSusChem*, 2008, **1**, 486-503.
11 T. Minowa and T. Ogi, *Catal. Today*, 1998, **45**, 411-416.
12 S. Li, L. Guo, C. Zhu and Y. Lu, *Int. J. Hydrogen Energy*, 2013, **38**, 9688-9700.
13 Y. Lu, S. Li, L. Guo and X. Zhang, *Int. J. Hydrogen Energy*, 2010, **35**, 7161-7168.
14 S. Li, Y. Lu, L. Guo and X. Zhang, *Int. J. Hydrogen Energy*, 2011, **36**, 14391-14400.
15 D. C. Elliott, L. J. Sealock Jr, E. G. Baker, *Ind. Eng. Chem. Res.*, 1993, **32**, 1542-1548.
16 P. Azadi, E. Afif, F. Azadi and R. Farnood, *Green Chem.*, 2012, **14**, 1766-1777.
17 L. Zhang, P. Champagne and C. Xu, *Int. J. Hydrogen Energy*, 2011, **36**, 9591-9601.
18 A. Sharma, H. Nakagawa and K. Miura, *Fuel*, 2006, **85**, 2396-2401.
19 A. J. Byrd, S. Kumar, L. Kong, H. Ramsurn and R. B. Gupta, *Int. J. Hydrogen Energy*, 2011, **36**, 3426-3433.
20 V. Nichele, M. Signoretto, F. Menegazzo, I. Rossetti and G. Cruciani, *Int. J. Hydrogen Energy*, 2014, **39**, 4252-4258.
21 I. Rossetti, A. Gallo, V. Dal Santo, C. L. Bianchi, V. Nichele, M. Signoretto, E. Finocchio, G. Ramis and A. Di Michele, *Chemcatchem*, 2013, **5**, 294-306.
22 I. Rossetti, J. Lasso, E. Finocchio, G. Ramis, V. Nichele, M. Signoretto and A. Di Michele, *Appl. Catal., A*, 2014, **477**, 42-53.
23 D. Chen, K. O. Christensen, E. Ochoa-Fernandez, Z. X. Yu, B. Totdal, N. Latorre, A. Monzon and A. Holmen, *J. Catal.*, 2005, **229**, 82-96.
24 K. O. Christensen, D. Chen, R. Lodeng and A. Holmen, *Appl. Catal., A*, 2006, **314**, 9-22.
25 M. Sasaki, Z. Fang, Y. Fukushima, T. Adschiri and K. Arai, *Ind. Eng. Chem. Res.*, 2000, **39**, 2883-2890.
26 K. P. Lopes, L. S. Cavalcante, A. Z. Simoes, J. A. Varela, E. Longo and E. R. Leite, *J Alloy Compd*, 2009, **468**, 327-332.
27 M. R. Mohammadi and D. J. Fray, *Solid State Sci.*, 2010, **12**, 1629-1640.
28 J. X. Chen, N. Yao, R. J. Wang and J. Y. Zhang, *Chem. Eng. J.*, 2009, **148**, 164-172.
29 X. Meng, H. Cheng, S.-i. Fujita, Y. Hao, Y. Shang, Y. Yu, S. Cai, F. Zhao and M. Arai, *J. Catal.*, 2010, **269**, 131-139.
30 A. V. Murugan, V. Samuel, S. C. Navale and V. Ravi, *Mater. Lett.*, 2006, **60**, 1791-1792.
31 M. J. Lazaro, Y. Echegoyen, C. Alegre, I. Suelves, R. Moliner and J. M. Palacios, *Int. J. Hydrogen Energy*, 2008, **33**, 3320-3329.
32 K. S. W. Sing, D. H. Everett, R. A. W. Haul, L. Moscou, R. A. Pierotti, J. Rouquerol and T. Siemieniewska, *Pure & Appl. Chem.*, 1985, **57**, 603-619.
33 F. L. P. Resende and P. E. Savage, *Energy Fuels*, 2009, **23**, 6213-6221.
34 F. L. P. Resende and P. E. Savage, *Aiche J*, 2010, **56**, 2412-2420.
35 F. L. P. Resende, M. E. Neff and P. E. Savage, *Energy Fuels*, 2007, **21**, 3637-3643.
36 Y. J. Lu, L. J. Guo, X. M. Zhang and Q. H. Yan, *Chem. Eng. J.*, 2007, **131**, 233-244.

View Article Online
DOI: 10.1039/C5RA12025J


37 O. S. Mitsumasa Osada, Kunio Arai, Masayku Shirai, *Energy Fuels*, 2006, **20**, 2337-2343.
38 R. M. Ravenelle, J. R. Copeland, W.-G. Kim, J. C. Crittenden and C. Sievers, *ACS Catal.*, 2011, DOI: 10.1021/cs1001515, 552-561.
39 R. M. Ravenelle, F. Z. Diallo, J. C. Crittenden and C. Sievers, *ChemCatChem*, 2012, **4**, 492-494.
40 S. N. Reddy, S. Nanda, A. K. Dalai and J. A. Kozinski, *Int. J. Hydrogen Energy*, 2014, **39**, 6912-6926.
41 C. Wu and P. T. Williams, *Appl. Catal., B*, 2010, **96**, 198-207.